THESIS FOR THE DEGREE OF LICENTIATE OF ENGINEERING

Nitrogen and Water in High Temperature Corrosion

Insights from First Principle Calculations

VEDAD BABIĆ

Department of Chemistry and Chemical Engineering
CHALMERS UNIVERSITY OF TECHNOLOGY

Göteborg, Sweden 2017

Nitrogen and Water in High Temperature Corrosion
Insights from First Principle Calculations
VEDAD BABIĆ

© VEDAD BABIĆ, 2017

Thesis for the degree of Licentiate of Engineering
Nr: 2017:21
Department of Chemistry and Chemical Engineering
Chalmers University of Technology
SE-412 96 Göteborg
Sweden
Telephone: +46 (0)31-772 1000

Chalmers Reproservice
Göteborg, Sweden 2017

Nitrogen and Water in High Temperature Corrosion
Insights from First Principle Calculations
Thesis for the degree of Licentiate of Engineering
VEDAD BABIĆ
Department of Chemistry and Chemical Engineering
Chalmers University of Technology

Abstract

Service life-time of alloys used in high temperature applications is often limited by corrosion. FeCrAl(Re) alloys are partially designed to form a protective α-alumina oxide scale at elevated temperatures in order to mitigate further oxidation. The scale growth commonly follows a parabolic rate law, which under a Wagnerian setting depends on transport of charged species; ions, vacancies and electrons. Small amounts of reactive elements (Y, Zr, Hf) are added to the alloy to improve scale properties, while also inhibiting outward Al diffusion. The oxide growth thus depends on mobility of oxygen vacancies in the scale.

A FeCrAl(Re) alloy was exposed to a 95% N_2, 5% H_2, and low p(O_2) environment, usually used for heat-treatment, forming a predominantly protective alumina scale with nodular inclusions of chromia. Under said conditions the chromia rich nodules permeate nitrogen. Density functional theory (DFT) calculations show that reducing processes, owing to the relative stability of chromia and alumina, lead to a maintained coverage of coordinatively unsaturated sites (CUS) on chromia surfaces, acting as N_2 dissociation sites. Chromium oxy-nitrides were shown metastable, offering a path for nitrogen into the alloy. H_2O acts as the main oxidant in this environment. A quasi-Wagnerian context was explored in which hydrogen was preferentially disposed as H^- in oxygen vacancies in hydroxylated alumina grain boundaries.

Keywords: DFT, corrosion, alumina, chromia, hydrogen, nitridation

LIST OF PUBLICATIONS

This thesis consists of an extended summary and the following appended papers:

Paper A	C. Geers et al. Properties of Alumina/Chromia Scales in N2-Containing Low Oxygen Activity Environment Investigated by Experiment and Theory. *Oxidation of Metals* (2017). DOI: `10.1007/s11085-016-9703-3`
Paper B	V. Babic et al. Fates of Hydrogen During Alumina Growth Below Yttria Nodules in FeCrAl(RE) at Low Partial Pressures of Water. *Electrocatalysis* (Mar. 2017). ISSN: 1868-5994. DOI: `10.1007/s12678-017-0368-8`. URL: `https://doi.org/10.1007/s12678-017-0368-8`

Statement of author's contribution

Paper A is a larger paper which includes both experimental and theoretical work, where I performed the DFT calculations. Paper B, like paper A, includes an experimental part in addition to a larger part on modelling. I was involved in writing both papers, though only the part on theory when it comes to paper A and B.

CONTENTS

Abstract

List of publications

Contents

I Extended Summary 1

1 Introduction 1
1.1 Background 1

2 High temperature oxidation 3
2.1 Thermodynamics of Oxides 3
2.2 Oxide growth 4
2.2.1 Parabolic and sub-parabolic kinetics 4
2.2.2 Linear oxidation kinetics 7
2.2.3 Logarithmic oxidation kinetics. 7
2.2.4 Breakaway oxidation 8
2.3 Reactive element effect 8

3 Experimental Techniques 11
3.1 Exposures 11
3.2 Analysis techniques 11
3.2.1 Scanning electron microscopy 11
3.2.2 Ion milling 12

4 Quantum Chemistry 15
4.1 Schrödinger equation 15
4.2 Computational Quantum Chemistry 16
4.2.1 The Hartree-Fock Method 16
4.3 Density Functional Theory 18
4.3.1 Exchange-correlation functional 21
4.3.2 Basis sets 22
4.3.3 Pseudopotentials 22

5 Model systems and computational details 25
5.1 Software description 25
5.2 A. Properties of alumina/chromia scales in N2-containing low oxygen activity environment investigated by experiment and theory 25
5.2.1 Method validation 25
5.3 B. Fates of hydrogen during alumina growth at low partial pressures of water 28

6 Results and Discussion 33
6.1 Exposure results 33
6.2 Properties of alumina/chromia scales in N2-containing low oxygen activity environment investigated by experiment and theory 33
6.2.1 Necessary conditions for N2 dissociation 34
6.2.2 Nitrogen incorporation through chromia scales 35
6.3 Fate of hydrogen in hydroxylated alumina grain-boundaries 35

7 Summary and future work 41

References 43

II Appended Papers 47

Part I

Extended Summary

1 Introduction

1.1 Background

Corrosion and oxidation phenomena are prevalent in today's society. Few examples include stainless kitchen utensils, cars exposed to varying environments spanning from the combustion conditions in the engine to the varying our-doors climate, fuel cells that power electric vehicles, and power plants utilizing high temperature corrosion resistant alloys. The present study addresses oxidation processes on a fundamental level, this way not only will the specific field benefit from the research, but indirectly, oxidation research in general is improved also by the generic insights gained.

Corrosion is mitigated by the design of alloys to form protective oxide scales suitable for each particular application. Stainless steels, for example, contain chromium which forms a non-rusting chromia scale. The applications stretch a wide range of temperatures; from oxidation at ambient temperatures to several hundred degrees at the inlets of steam turbines in heat engines of power plants. It becomes important to understand on a fundamental level the different types of corrosion processes involved, in order to create new longer-lasting and more durable materials. Not only oxygen may act as an oxidant but also e.g. sulphur and carbon. Even nitrogen N_2, which is usually considered to be inert, is found to act as oxidant at low oxygen-high nitrogen partial pressures, thus reducing the alloy life-time by forming various metal nitrides.

The underlying processes involved in high temperature oxidation are mainly transport controlled; ion, electron and hole transport are all necessary to take into consideration when researching new materials and their oxides. To arrive at a fundamental understanding, a theoretical approach is required and this may involve e.g. first-principle calculations employing atomistic models.

The context of the present work is provided by the FeCrAl alloys containing small amounts of reactive elements (RE, e.g. Y, Zr, and Hf, which have been shown to improve scale properties) being subjected to a 95% N_2, 5% H_2 environment with ppm content of water at 900°C. In this environment, both chromia and alumina are thermodynamically stable and the alloy forms a thin protective α-alumina scale with chromia nodules as found by electron microscopy. Analysis showed the chromia nodules to permeate nitrogen and form nitrides beneath this scale. Density functional theory (DFT) studies were employed to explain (a) why chromia nodules permeate nitrogen, and (b) the fate of hydrogen at hydroxylated alumina interfaces when water acts as main oxidant.

2 High temperature oxidation

Good corrosion resistance and long-term mechanical durability (strength, creep) are necessary prerequisites to ensure the usefulness of a commercial high-temperature alloy over time. The degradation of high temperature alloys occurs through various corrosive processes often involving so-called break-away oxidation. Interestingly, oxidation offers a main means to resist corrosion, i.e. by forming a dense, slowly growing oxide scale which protects the underlying metal from further oxidation. In alumina forming alloys at high temperatures, this protective oxide scale is α-Al_2O_3 (corundum), the thermodynamically most stable aluminium-oxide. It is usually said to form above 900 °C [3] but has been reported to form in temperatures as low as 700 °C [4]. Transient alumina scales, such as γ-Al_2O_3 and θ-Al_2O_3 are formed at lower temperatures [5, 6]. In the following sections, the thermodynamics and oxide growth mechanisms are elaborated upon.

2.1 Thermodynamics of Oxides

All non-noble metals form an oxide layer in air. Some oxides may form transient oxide layers first which gradually rearranges into a thermodynamically more stable structure. A general oxide formation reaction can be expressed as:

$$xM(s) + \frac{y}{2}O_2(g) \rightarrow M_xO_y \tag{2.1}$$

and is associated with a change in Gibb's free energy, ΔG. The free energy can be expressed as the energy difference between products and reactants:

$$\Delta G = \sum \Delta G_{products} - \sum \Delta G_{reactants} \tag{2.2}$$

The change in Gibb's free energy can also be expressed as a function of temperature (T), the gas constant (R), and the reaction quotient (Q_r):

$$\Delta G = \Delta G^0 + RTlnQ_r \tag{2.3}$$

$$Q_r = \frac{a(M_xO_y)}{a(M)^x a(O_2)^{\frac{y}{2}}}|_t \tag{2.4}$$

where Q_r is a product of activities at time t before equilibrium has been established and is related to the equilibrium constant by taking Q_r at infinite time, $K_{eq} = Q_r|_{t=\infty}$. At equilibrium, $\Delta G = 0$:

$$\Delta G^0 = -RTlnK_{eq} = -RTln\frac{a(M_xO_y)}{a(M)^x a(O_2)^{\frac{y}{2}}} \tag{2.5}$$

In an ideal case, following Raoult's law, the activity of a solid is assumed to be identity while the activity of a gas is assumed to be it's partial vapor pressure p_i. Applied to eq. (2.1), the Gibb's free energy is estimated to be

$$\Delta G^0 = -RTln(p_{O_2}) \tag{2.6}$$

Given that ΔG^0 is known, the lowest partial pressure of oxygen at which the oxide is stable, the dissociation pressure, can be calculated by solving eq. (2.6) for p_{O_2};

$$p_{O_2} = (e^{-\frac{\Delta G^0}{RT}}) \tag{2.7}$$

The oxygen partial pressure is plotted against temperature (T-ΔG^0) in an Ellingham diagram, see Fig. 2.1. It is possible to compare the relative stabilities of oxides at chosen temperatures. The temperature dependence can be illustrated by rewriting eq. (2.2) as a function of enthalpy, H, and entropy, S:

$$\Delta G^0 = \Delta H - T\Delta S \tag{2.8}$$

The slope in the Ellingham diagram is then $-\Delta S$ while the Gibb's free energy at $T = 0$ K is the enthalpy of the reaction, ΔH.

2.2 Oxide growth

Initially, oxide nucleates on the alloy surface and grows laterally until a thin film is formed. Depending on the scale formed, and the environment under which the oxide grows, various types of growth kinetics are obtained. In the following sections, four types of oxidation kinetics are elaborated upon, linear, (sub-)parabolic, logarithmic, and breakaway oxidation. The detailed description is reserved for Wagnerian kinetics (Sec. 2.2.1) which serves as the contextual framework under which the calculations in this thesis were performed i.e. where oxide growth is limited by diffusion of ionic species. The different types of oxidation kinetics are illustrated in Fig. 2.2.

For the oxide to grow, ionic species must diffuse through the oxide scale. At low temperatures (below half the melting temperature [7]), diffusion is considered to be mainly composed of short-circuit diffusion [8] i.e. line or planar defects (grain boundaries). In this work line defect diffusion is omitted as the oxides under study (chromia and alumina) are relatively dense and stable. Grain boundary diffusion is considered to be the dominant diffusion path due to a lower activation energy. At higher temperatures, grain boundary diffusion is less dominant as grain sizes increase (thus fewer grain boundaries), but also because the thermal energy increases (average kinetic energy, $\frac{3}{2}kT$, at room temperature is around 35 meV and 0.2 eV at 1200 °C) which would mitigate bulk-diffusion which otherwise has a higher activation energy (25-40% higher) [8].

Alumina growth on FeCrAl alloys at high temperatures (>900 °C) is dominated by short-circuit diffusion [9, 10] although it is not clear whether aluminium or oxygen transport dominates [11].

2.2.1 Parabolic and sub-parabolic kinetics

Parabolic oxidation kinetics were derived as early as 1920 by Tammann [12], and in 1923 by Pilling and Bedworth [13] under the assumption that the diffusing species were neutral. Wagner (1933) on the other hand assumed that the oxidation process was limited by the diffusion of ionic species i.e. cations, anions, and electrons. Wagner also assumed

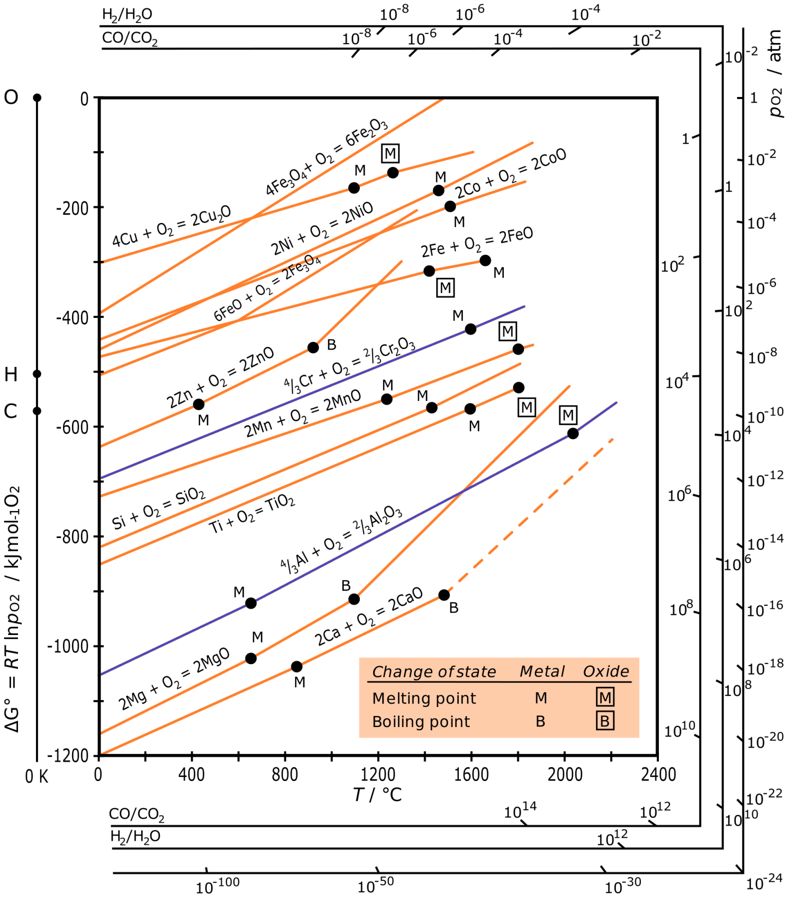

Figure 2.1: Ellingham diagram showing standard free energy of formation plotted against temperature for selected oxides. The line plots for chromia and alumina are highlighted in blue color, as they are of importance for the work presented in this thesis.

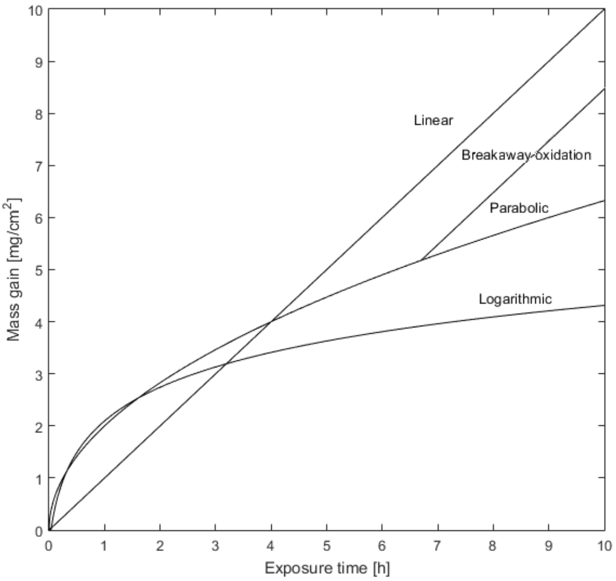

Figure 2.2: Mass gain curves illustrating linear, parabolic, logarithmic and breakaway oxidation kinetics. In this case, breakaway oxidation occurs after a certain amount of time where e.g. a non-protective Fe_2O_3 scale is formed and linear oxidation kinetics are obtained.

local thermodynamic equilibrium to be established at every point throughout the scale, including interfaces. When the Wagnerian approach is coupled with the assumption that diffusion occurs mainly in the lattice, parabolic oxidation kinetics are obtained, see Eq. 2.9 and 2.10.

$$\frac{dx}{dt} = k_p \frac{1}{x} \tag{2.9}$$

$$\Delta m^2 = k_p t \tag{2.10}$$

where k_p is the parabolic oxide rate constant, and Δm is the mass change [5, 11]. This approach has shown to predict the oxidation behaviour quantitatively of CuO_2 and CoO_4 [14].

Alumina grows predominantly through grain boundary diffusion, the kinetics being parabolic [15] or sub-parabolic [16, 17]. Sub-parabolic kinetics are obtained when, during the oxide growth e.g. grain size increases, decreasing number of diffusion paths or, when the activation energy of diffusion increases with oxide thickness. Sub-parabolic (cubic) oxide growth is defined as:

$$\Delta m^3 = k_c t \tag{2.11}$$

where k_c is a cubic oxide rate constant. Note that the parabolic and cubic rate constants do not have the same units and are as such not directly comparable.

2.2.2 Linear oxidation kinetics

When the mass gain is constant in time, see Eq. 2.12 , linear kinetics are derived.

$$\Delta m = kt \tag{2.12}$$

This type of kinetics are obtained under conditions where diffusion of species through the scale is not rate limiting e.g. where surface or phase-boundary processes limit the oxidation rate [18] or when the oxide thickness remains constant.

2.2.3 Logarithmic oxidation kinetics.

Logarithmic kinetics are defined by the following equation:

$$\Delta m = k \ln(t + t_0) + C \tag{2.13}$$

where k and C are constants. Logarithmic mass gain is typically obtained at lower temperatures and in thin oxides, where electrons can tunnel through the oxide scale. An electric field is established across the thin scale which drives the diffusion process of charged species. As the scale grows, the electric field is effectively shielded and e.g. Wagnerian oxidation kinetics may be obtained.

It may also be derived by assuming that the activation energy, W, for the mechanism by which ions move to be of the form:

$$W = W_0 + \mu x \tag{2.14}$$

where μ is a constant characteristic of the oxide. As the oxide grows, the activation energy for diffusion increases, leading to a decreased diffusivity. The growth rate can be expressed on the following form:

$$\frac{dx}{dt} = c \times exp[\frac{-(W_0 + \mu x)}{kT}] \tag{2.15}$$

which integrates to a logarithmic function:

$$x = A \times ln(1 + Bt) \tag{2.16}$$

This type of oxidation kinetics are also called Cabrera-Mott kinetics [19, 20].

2.2.4 Breakaway oxidation

Breakaway oxidation or chemical failure is a term used to denote different kinds of failure during the oxidation process. Considering that the alloy is continuously being depleted of the oxidizing element, a certain point may be reached when formation of a non-protective oxide scale is thermodynamically favored. This type of breakaway behaviour is called intrinsic chemical failure. Additionally, spalling and cracking of the oxide scale may lead to mechanically induced chemical failure (MICF) [21].

2.3 Reactive element effect

It is well known that addition of reactive elements (Zr, Y, La, Ce, Sc, etc.), RE improve the adherence of the scale as well as decrease the oxide scale growth rate [3, 8, 9]. It has been experimentally verified with transmission electron microscopy (TEM) that a large number of these cation dopants are segregated not only to the grain boundaries but also to the metal-scale interface [22]. The role that the RE play at grain boundaries or interfaces are still under debate and many different mechanisms have been proposed. In α-Al_2O_3, RE decrease the outward diffusivity of Al, possibly by blocking diffusion paths, sometimes referred to as a steric effect [11]. Other RE effects include reducing the so called sulfur effect, where sulfur segregates to the metal/scale interface and causes spallation [23].

In alumina formers it has been found that it is crucial (but not sufficient) for the RE to segregate to grain boundaries in order to provide a positive effect on the oxidation resistance. The ion size needs to be large enough in order to induce a steric effect which inhibits the cation outward diffusion. Ti for example is highly segregated to the grain boundaries but (supposedly) due to its smaller size, does not lead to a significant effect on the oxide growth [22, 10].

3 Experimental Techniques

There are various experimental techniques employed in order to investigate oxidation mechanisms. They include mass gain, spectrometry, microscopy, and exposure techniques. The experimental work covered in this thesis has been performed by C. Geers and a short summary and overview of the techniques employed is presented in the following sections.

3.1 Exposures

The exposures were performed in horizontal furnace tubes, in which small polished samples, ca $10x10x1$ mm^3, are exposed for typically 1-1000 h. A high precision scale, typically 1 microgram precision, is used in conjunction with exposures in order to measure any mass change, which can be used to decide the oxidation kinetics. The gaseous environment is controlled and designed for the specific experiment and the temperature can be kept constant or cycled. Cycling experiments may induce cracking of the oxide scales as the alloy is cooled off and re-heated repeatedly, leading to the scale spalling off.

3.2 Analysis techniques

Analysis techniques commonly employed in state-of-the art corrosion research includes optical microscopy, scanning electron microscopy (SEM) and transmission electron microscopy (TEM). These techniques can be used in conjunction with mechanical polishing or techniques employing focused or broad ion beams (FIB/BIB) in order to image a surface or cross-section. In this work, SEM will be presented together with the two ion milling techniques.

3.2.1 Scanning electron microscopy

Usually abbreviated SEM, scanning electron microscopy is an often used imaging tool to characterize the oxidation behaviour of metals. High resolution images are produced by sweeping an electron beam over a sample, good for microstructure and topography analysis. With SEM it is possible to analyze back-scattered and secondary electrons, as well as emitted x-rays during the sweeping process.

When the incoming beam back-scatters elastically, a Z-contrast is achieved as heavier elements provide a higher probability of back-scattering i.e areas with heavier elements are lighter than those with lighter elements. This analysis may be used to identify compositional differences.

Secondary electrons are electrons which have been excited by the (primary) electron beam and emitted during the scanning process. These electrons are usually emitted from the atoms on the top surface of the sample and give more topological information compared to back-scattered imaging.

If the SEM machine is coupled with x-ray detectors, it is possible to analyze the emitted x-rays and perform energy-dispersive x-ray spectroscopy (EDX) to obtain the composition in the sample.

3.2.2 Ion milling

In order to generate a clear image in the SEM it is important to prepare the samples. There are two milling techniques that will be mentioned here, focused ion beam (FIB) and broad ion beam (BIB) milling. FIB uses a beam of accelerated gallium ions and may be used in conjunction with SEM to simultaneously image and mill a sample, then called a FIB-SEM. The milling is on the micrometer scale in order to perform cross-sectional analysis. Instead of milling the sample with a FIB, it is possible to cut the sample of interest in two parts and then use a BIB to polish the cross-section. As the beam is broader, it works on a millimeter scale instead.

4 Quantum Chemistry

Quantum chemistry is the application of quantum mechanics to problems in chemistry. It is possible to calculate properties of chemical systems e.g. vibrational mode frequencies and intensities, which can be measured by e.g. infrared (IR) and Raman spectroscopy. The basis of quantum mechanics is the Schrödinger equation which was introduced by Erwin Schrödinger in 1926 [24].

In general it is not possible to solve the Schrödinger equation exactly (with one exception, the hydrogen atom), especially when dealing with many-electron systems like molecules or materials. In the following sections, two computational methods for solving the Schrödinger equation are covered, the Hartree-Fock method which dates back to the late 1920s and Density Functional Theory (DFT) which builds on Hartree-Fock and which was employed in this work.

4.1 Schrödinger equation

The more general, time-dependent Schrödinger equation describes how a quantum mechanical state, $\psi(x,t)$ evolves in time, and is postulated to be (for a one-particle, one-dimensional system):

$$i\hbar\frac{\partial\psi(x,t)}{\partial t} = -\frac{\hbar^2}{2m}\frac{\partial^2\psi(x,t)}{\partial x^2} + V(x,t)\psi(x,t) \tag{4.1}$$

where $\hbar$ is the reduced Planck's constant, $V(x,t)$ is the potential-energy function of the system and m is the mass of the particle. Not many quantum mechanical applications use this form of the Schrödinger equation. It is often instead the simpler, time-independent form which is used. It is derived by assuming that the potential-energy function, V is not a function of time, but only position. In that case a time-independent form of Eq. 4.1 is found by variable seperation, $\psi(x,t) = \psi(x)f(t)$. The equation is then rearranged so that the left-hand-side only depends on position and the right hand side only depends on time. The both sides must then be equal to a constant, E and the time-independent equation is found to be:

$$-\frac{\hbar^2}{2m}\frac{d^2\psi(x)}{dx^2} + V(x)\psi(x) = E\psi(x) \tag{4.2}$$

where E is postulated to be the energy of the system. This equation can be rewritten as

$$\hat{H}\psi(x) = E\psi(x) \tag{4.3}$$

where $\hat{H}$ (the Hamiltonian) is an operator containing all the forces and interactions acting within the system, in this case kinetic energy and an external potential, $V(x)$ acting on the single particle.

4.2 Computational Quantum Chemistry

The system of interest here is a material consisting of nuclei and electrons. The Hamiltonian for such a system can be described as:

$$\begin{aligned}\hat{H} &= \hat{T}_{nuc} + \hat{V}_{N-N} + \hat{H}_{el} = \\ &= \underbrace{-\sum_{A} \frac{\nabla_A^2}{2M_A}}_{\hat{T}_{nuc}} + \underbrace{\sum_{A<B} \frac{Q_A Q_B}{|\mathbf{R}_A - \mathbf{R}_B|}}_{\hat{V}_{N-N}} \underbrace{- \sum_{a} \frac{1}{2}\nabla_a^2 + \sum_{a<b} \frac{1}{|\mathbf{r}_a - \mathbf{r}_b|} - \sum_{a,A} \frac{Q_A}{|\mathbf{R}_A - \mathbf{r}_a|}}_{\hat{H}_{el}}\end{aligned} \tag{4.4}$$

where $\hat{T}_{nuc}$ is the kinetic energy of the nuclei, $\hat{V}_{N-N}$ is the coulomb interaction between the nuclei and $\hat{H}_{el}$ is the electronic Hamiltonian, consisting of kinetic energy terms for the electrons as well as electron-electron and electron-nucleus coulomb interactions. A and B are indices of nuclei, and a and b are indices of electrons. The **R** are coordinates of nuclei and **r** are electron coordinates. Atomic units will be assumed i.e. $\hbar = m_e = q_e = \frac{1}{4\pi\epsilon_0} = 1$.

The many-body wave-function becomes too complicated in these systems due to electron correlation and several approximations are necessary in order to solve the Schrödinger equation. The first is the **Born-Oppenheimer** approximation [25] which assumes that the mass of the nuclei are much larger than the electron mass so that the nuclei can be assumed to be stationary with respect to the motion of the electrons. It follows that the motions of nuclei and electrons can be solved separately i.e.:

$$\psi_{BO}(\mathbf{r}, \mathbf{R}) = \phi(\mathbf{R})\chi(\mathbf{r}, \mathbf{R}) \tag{4.5}$$

The kinetic energy of the nuclei, T_{nuc} depend only on the coordinates of the nuclei and can thus be treated separately from the electrons. The electronic energy E_{el} can be obtained from the electronic Hamiltonian H_{el} and the electronic wave function χ:

$$\hat{H}_{el}\chi(\mathbf{r}, \mathbf{R}) = E_{el}\chi(\mathbf{r}, \mathbf{R}) \tag{4.6}$$

The nuclear wave-function $\phi(\mathbf{R})$ is a solution to:

$$(\hat{T}_{nuc} + E_{el} + \hat{V}_{N-N})\phi(\mathbf{R}) = E_{nuc}\phi(\mathbf{R}) \tag{4.7}$$

Note that the Born-Oppenheimer approximation does not hold if movements of the nuclei cause transitions between electron states, in that case, wave-function separation is not possible.

4.2.1 The Hartree-Fock Method

To compute the wave-function for many-body systems, the Born-Oppenheimer approximation is not enough. The Hartree-Fock method was first introduced by Hartree [26, 27] and improved by Fock [28] and Slater[29]. In this method electrons are assumed to be independent and non-coupled, thus the wave-function can be expressed as a product of one-electron spin-orbitals $\phi_i(\mathbf{r}_i)$.

$$\psi(\mathbf{r}_1, \mathbf{r}_2, \mathbf{r}_3, ..., \mathbf{r}_n) = \prod_i \phi_i(\mathbf{r}_i) \tag{4.8}$$

The reason for including spin is that electrons, which are fermions (particles with half-integer spin) must obey the Pauli principle, and from quantum mechanical principles, any real wave-function that should represent a system of fermions must be anti-symmetric with respect to exchange of particles. This property is taken into account by expressing the wave-function as a Slater determinant [30]:

$$\psi = (N!)^{-1/2} \begin{vmatrix} \phi_1(\mathbf{r}_1) & \phi_2(\mathbf{r}_1) & \cdots & \phi_n(\mathbf{r}_1) \\ \phi_1(\mathbf{r}_2) & \phi_2(\mathbf{r}_2) & \cdots & \phi_n(\mathbf{r}_2) \\ \vdots & \vdots & \ddots & \vdots \\ \phi_1(\mathbf{r}_n) & \phi_2(\mathbf{r}_n) & \cdots & \phi_n(\mathbf{r}_n) \end{vmatrix} \tag{4.9}$$

The energy of such a wave-function is given by the expectation value of the exact non-coupled Hamiltonian:

$$E = \langle \psi | \hat{H} | \psi \rangle \tag{4.10}$$

In the electronic Hamiltonian, $\hat{H}_{el}$ from Eq. (4.4), it is possible to identify one-electron (h_a) and two-electron (g_{ab}) terms:

$$\hat{H} = -\sum_{a}^{N} \underbrace{\Big(\frac{1}{2}\nabla_a^2 - \sum_{A} \frac{Q_A}{|\mathbf{R}_A - \mathbf{r}_a|}\Big)}_{h_a} + \sum_{a<b}^{N} \underbrace{\frac{1}{|\mathbf{r}_a - \mathbf{r}_b|}}_{g_{ab}} \tag{4.11}$$

where N is the number of electrons. Since the electrons are assumed to be independent, only one-electron orbitals need to be known. To do this, the one-electron orbitals are expressed in a known basis function χ_μ:

$$\phi_i(\mathbf{r}) = \sum_{\mu}^{N} c_{i\mu}\chi_\mu(\mathbf{r}) \tag{4.12}$$

where N is the size of the basis set. This can be re-written on the following form, as the so called **Hartree-Fock equation**:

$$\underbrace{\Big(-\frac{\nabla^2}{2} \underbrace{- \sum_{A} \frac{Q_A}{|\mathbf{R}_A - \mathbf{r}|}}_{V_{ext}} + 2\hat{J} - \hat{K} \Big)}_{\hat{F}} \phi(\mathbf{r}) = \epsilon_i \phi(\mathbf{r}) \tag{4.13}$$

$$\hat{J}_j(1) f(1) = f(1) \int |\phi_j(2)|^2 \frac{1}{r_{12}} dv_2 \tag{4.14}$$

$$\hat{K}_j(1) f(1) = \phi_j(1) \int \frac{\phi_j^*(2) f(2)}{r_{12}} dv_2 \tag{4.15}$$

where $\hat{F}$ is the Fock-operator, $\hat{J}$ is the Coulomb operator, $\hat{K}$ is the exchange operator, ϵ_i are orbital energies and f is an arbitrary function. The goal of this method is to find orbitals ϕ_i which minimize the energy in Eq. (4.10) under the condition that the basis set is orthonormal.

Using Eq. (4.12) and substituting it in the Hartree-Fock equation (4.13), and multiplying with χ_r^* leads to:

$$\sum_{\mu=1}^{N} c_{\mu i}(F_{r\mu} - \epsilon_i S_{r\mu}) = 0, \quad r = 1, 2, ...N \tag{4.16}$$

$$F_{r\mu} \equiv \langle \chi_r | \hat{F} | \chi_\mu \rangle, \quad S_{r\mu} \equiv \langle \chi_r | \chi_\mu \rangle \tag{4.17}$$

This leads to a set of linear homogenous equations called the (**Hartree-Fock-**)**Roothaan equations** and are solved iteratively on matrix form:

$$\mathbf{FC} = \mathbf{SC}\epsilon \tag{4.18}$$

The total electronic energy is then expressed as:

$$E_{el} = \sum_{i}^{N} \langle \phi_i | \hat{h} | \phi_j \rangle + \frac{1}{2} \sum_{ij}^{N} \left\{ \underbrace{\langle \phi_i \phi_j | \frac{1}{r_{12}} | \phi_i \phi_j \rangle}_{\text{Coulomb term}} - \underbrace{\langle \phi_i \phi_j | \frac{1}{r_{12}} | \phi_j \phi_i \rangle}_{\text{exchange term}} \right\} \tag{4.19}$$

This method allows for the energy of a many-body system to be calculated, although being computationally demanding. It scales as N^4 where N is the size of the basis set.

4.3 Density Functional Theory

Instead of trying to find the one-electron wave-functions and thus creating the systems wave-function, it is possible to first try to find the overall electron density, $\rho(\mathbf{r})$ which is then simply correlated to the wave function through

$$\rho(\mathbf{r}) = \psi^*(\mathbf{r})\psi(\mathbf{r}) = |\psi(\mathbf{r})|^2 \tag{4.20}$$

This is the basis of Density Function Theory (DFT) and it reduces the spatial dependence of the problem from finding 3N spatial coordinates (3 for each electron) to only 3 (the electron density only depends on three space-coordinates e.g. x,y,z). The advantage of this method is that DFT nominally scales as N^2 (compare to N^4 for Hartree-Fock).

The basis of DFT lies on two **Hohenberg-Kohn** theorems which state that:

- The ground state electron density $\rho_0(\mathbf{r})$ is uniquely determined by the external potential $v_{ext}(\mathbf{r})$.

$$v_{ext}(\mathbf{r}) \xleftrightarrow{1-1} \rho_0(\mathbf{r}) \tag{4.21}$$

- The existence of an energy functional $E_{HK}[\rho]$ (HK for Hohenberg-Kohn) with two properties:

$$E_{HK}[\rho_0] = E_0 \tag{4.22}$$

$$E_{HK}[\rho] > E_0, \text{ for } \rho \neq \rho_0 \tag{4.23}$$

The energy functional, $E_{HK}[\rho]$ is given by:

$$E_{HK}[\rho] = \underbrace{\int v_0(\mathbf{r})\rho(\mathbf{r})d^3\mathbf{r}}_{E_{ext}[\rho]} + \underbrace{\int \psi^*[\rho]\Big(\hat{T}+\hat{U}\Big)\psi[\rho]d^3\mathbf{r}}_{F[\rho]} \tag{4.24}$$

Here, $F[\rho]$ is universal, since it contains electron kinetic energy and electron-electron interactions. The system specific term is the first part of Eq. (4.24), the external potential v_0 which contains the interaction between electrons and nuclei. The ground state density ρ_0 is found by solving the Euler-Lagrange equation

$$\left.\frac{\delta E_{HK}[\rho]}{\delta\rho(\mathbf{r})}\right|_{\rho=\rho_0} = 0 \tag{4.25}$$

In DFT, it is assumed that the system is *v-representable* i.e. if $v_0(\mathbf{r})$ (for interacting particles) corresponds to a ground state $\rho_0(\mathbf{r})$ then there exists an effective local potential $v_{KS,0}(\mathbf{r})$ (KS = Kohn-Sham) for non-interacting particles that corresponds to the same ground state density. It is then possible to calculate the exact energy of the ground state using a non-interaction approximation and solving the **Kohn-Sham equation** [31]:

$$\Big(-\frac{\nabla^2}{2} + V_{ext}(\mathbf{r}) + \underbrace{\int \frac{\rho(\mathbf{r})}{|\mathbf{r}-\mathbf{r'}|}d^3\mathbf{r'}}_{v_H} + V_{xc}[\rho]\Big)\phi_i(\mathbf{r}) = \epsilon_i\phi_i(\mathbf{r}) \tag{4.26}$$

where ϕ_i is a Kohn-Sham orbital (orbital describing the non-interacting system, see Hartree-Fock) with energy ϵ_i and v_H is the Hartree potential describing classical electron-electron Coulomb interactions. Compare the Kohn-Sham equation with the Hartree-Fock equation (Eq. 4.13), the difference is that the Hartree-Fock exchange term is replaced by an exchange-correlation term in DFT. In practice this means that DFT does not have an exact exchange term, which Hartree-Fock has, but it includes an electron correlation term which is not described in Hartree-Fock. The ground-state density is given as a sum over all occupied Kohn-Sham orbitals

$$\rho_0 = \sum_i^N |\phi_i|^2 \tag{4.27}$$

Rewriting Eq. (4.24) leads to an expression which can be solved iteratively, using the same procedure as the Hartree-Fock method, see Fig. 4.1 for a flow-chart:

$$E[\rho] = \int v_{KS,0}(\mathbf{r})\rho(\mathbf{r})d^3\mathbf{r} + \frac{1}{2}\int\int \frac{\rho(\mathbf{r})\rho(\mathbf{r'})}{|\mathbf{r}-\mathbf{r'}|}d^3\mathbf{r}d^3\mathbf{r'} + \sum_i^N\Big(\int \phi_i^*(-\frac{\nabla^2}{2})\phi_i d^3\mathbf{r}\Big) + E_{xc}[\rho] \tag{4.28}$$

Using the Kohn-Sham equation it is possible to calculate the kinetic, external, and electron-electron Coulomb energy terms exactly but not the exchange-correlation energy. For this, further approximations are necessary.

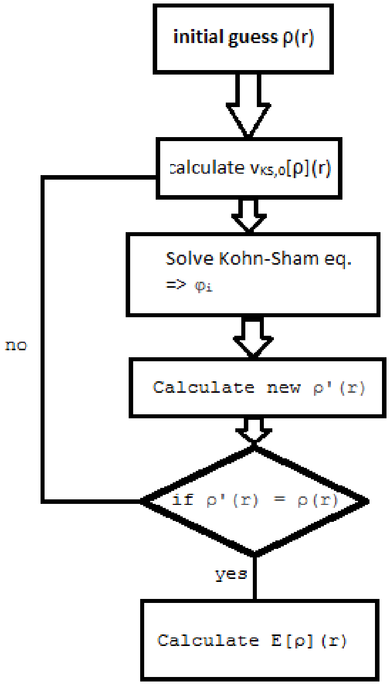
initial guess ρ(r)
calculate v_KS,0[ρ](r)
Solve Kohn-Sham eq.
=> φi
Calculate new ρ'(r)
if ρ'(r) = ρ(r)
no
yes
Calculate E[ρ](r)

Figure 4.1: A simple flow-chart of the iterative process that is employed in DFT codes to find the ground-state energy $E[\rho](r)$. Initially the electron density is guessed from which a Kohn-Sham potential is calculated for solving the Kohn-Sham equations. A new density is then calculated and compared to the previous density. This procedure continues until certain convergence criteria are met.

4.3.1 Exchange-correlation functional

The exchange-correlation functional E_{xc} is by definition:

$$E_{xc}[\rho] = F[\rho] - \frac{1}{2}\int\int \frac{\rho(\mathbf{r})\rho(\mathbf{r'})}{|\mathbf{r} - \mathbf{r'}|} d^3\mathbf{r} d^3\mathbf{r'} - T_S[\rho] \tag{4.29}$$

where T_S is the kinetic energy of non-interacting electrons. The total energy is obtained from the energy functional $E_{HK}[\rho]$ defined in Eq. (4.24) and $F[\rho]$ can be found from Eq. (4.29):

$$F[\rho] = T_S[\rho] + V_H[\rho] + E_{xc}[\rho] \tag{4.30}$$

It consists of four terms, the three above in addition to the external energy E_{ext} which is the energy contribution from the external field on the electrons. E_{xc} is the exchange-correlation energy including non-direct electron-electron interactions together with $F[\rho] - T_S[\rho]$ i.e. the difference between the T_S and the true kinetic energy of the electronic system. V_H is the Hartree energy from coulomb interactions.

There are many different ways to express the exchange-correlation functional $E_{xc}[\rho]$, and the choice can be crucial for the calculations that are performed. There is a vast sea of functionals that have been developed, some more complicated than others. The simplest model is the *Local Density Approximation* (LDA) which approximates the exchange-correlation term at point r with that of an electron gas with density $\rho(r)$[32]. When the functional is generalized to take spin into account, the Local Spin Density Approximation (LSDA) is arrived at, having following form:

$$E_{XC}^{LSDA}[n_\uparrow, n_\downarrow] = \int d^3r n(r)\epsilon_{XC}(n_\uparrow, n_\downarrow) \tag{4.31}$$

where $n = n_\uparrow + n_\downarrow$ is the total electron density and ϵ_{XC} is the exchange-correlation potential, which is an analytical expression parametrized to fit e.g. monte carlo data. An example is the LDA-PWC functional by Perdew and Wang[33].

LDA can be extended by including a dependence on the local density gradients, arriving at the Generalized Gradient Approximation (GGA), example functionals include Perdew-Wang 1991 (PW91) [34] and Perdew, Burke and Ernzerhof (PBE) [35]. GGA is usually expressed:

$$E_{XC}^{GGA}[n_\uparrow, n_\downarrow] = \int d^3r f(n_\uparrow, n_\downarrow, \nabla n_\uparrow, \nabla n_\downarrow) \tag{4.32}$$

where $f(n_\uparrow, n_\downarrow, \nabla n_\uparrow, \nabla n_\downarrow)$ is constructed as to satisfy certain physical conditions. PW91 was constructed as to satisfy as many exact conditions as possible, while PBE was constructed to satisfy only those that are energetically significant[35]. GGA computes atomic and molecular energies remarkably well, as it was designed for, but considering that some physical conditions are not met in the construction of the functional, other attributes are lost. Both LDA and GGA approximations are e.g. good for metallic systems which are strongly dislocalized, but in the case of localized systems, both underestimate the band-gap in metal oxides by several electron volts [36]. An improvement is to include an amount of exact exchange from Hartree-Fock which results in so called hybrid functionals. The most common hybrid functionals are the PBE0 [37] and B3LYP [38] functionals.

Two issues with DFT due to the approximated exchange-correlation functionals are the self-interaction error i.e. the fact that electrons feel repulsion from all electrons in the system, themselves included [36] and a static correlation error which is due to only using a single determinant to describe the wave-function, which works well for non-degenerate systems but not in the degenerate case [39].

4.3.2 Basis sets

As mentioned earlier (see Sec. 4.2.1), the wave functions are expanded in a basis set, but there are many possible basis sets to use. They include Slater functions [40], Gaussian functions [41], plane wave basis set [42] and numerical basis set. The systems studied in this thesis are solid crystalline materials which have translational symmetry. In this case, it is possible to expand the wave functions in a plane wave basis subject to a periodic potential according to Bloch's theorem :

$$\phi_j(\mathbf{r},\mathbf{k}) = e^{i\mathbf{kr}}u_j(\mathbf{r}) \tag{4.33}$$

and

$$u_j(\mathbf{r}) = \sum_{\mathbf{G}} C_{\mathbf{G},j}e^{i\mathbf{Gr}} \tag{4.34}$$

In principle, an infinite number of plane waves is needed to describe the system, but in practice an energy cut-off E_{cutoff} is introduced which defines the smallest length-scale of the system.

4.3.3 Pseudopotentials

Electrons are divided into two groups, core electrons and valence electrons. Core electrons screen the nuclear charge but their contribution to chemical bonds can be neglected. The core electrons are "frozen" and replaced by a pseudopotential. Only valence electrons are described explicitly. The pseudopotential is designed to be nodeless and equal to the real, all-electron orbital outside a chosen core-radius, R_C.

Norm-conserving potentials are those that fulfill the norm-conserving condition, i.e. that the real ($\phi_{\text{all electron}}$) and pseudo ($\phi_{\text{pseudopotential}}$) wave-function both generate the same charge-density:

$$\int_0^{R_C} |\phi_{\text{all electron}}|^2 d^3\mathbf{r} = \int_0^{R_C} |\phi_{\text{pseudopotential}}|^2 d^3\mathbf{r} \tag{4.35}$$

where R_C is the core radius. It can be found that it is not possible to create a smoother pseudopotential than the all-electron potential for e.g. O-2p orbitals under norm-conserving conditions. By allowing the pseudopotential to violate this condition, it becomes possible to form smoother potentials, so called ultrasoft pseudopotentials [43]. Often, when designing pseudopotentials, R_C is chosen to be smaller than the radial wave-function maximum but with ultrasoft potentials it is possible to choose R_C well beyond this maximum, reducing the needed cut-off energy to describe the system. In this work, ultrasoft pseudopotentials have been employed throughout.

5 Model systems and computational details

There are two papers included in this thesis:

A Geers C, Babic V, Mortazavi N, Halvarsson M, Jönsson B, Johansson L-G, Panas I and Svensson J-E. **Properties of Alumina/Chromia Scales in N_2-containing Low Oxygen Activity Environment Investigated by Experiment and Theory**

B Babic V, Geers C, and Panas I. **Fates of hydrogen during alumina growth below yttria nodules in FeCrAl(RE) at low partial pressures of water**

The models and computational parameters employed in each paper will be elaborated in the following sections.

5.1 Software description

The calculations in this work were performed using the CASTEP code within the Materials studio 6.0 suite. CASTEP is a commercial Density Functional Theory (DFT) code which is used to compute electronic structures of periodical systems. The code relies on pseudopotentials to express the inert core region of the atoms while the valence electrons are treated explicitly. Periodic boundary conditions are used to simulate an infinitely large crystal. The electronic orbitals are expanded in a plane-wave basis including all plane waves up to a chosen kinetic energy E_{cut} such that $\hbar^2 k^2/2m < E_{cut}$, where k is the wave vector and m is the electron mass. The Brillouin zone is sampled with the Monkhorst-Pack scheme, and the exchange-correlation energy is approximated using a generalised gradient functional proposed by Perdew et al. (GGA-PBE). The simulations are spin-polarized when mentioned.

5.2 A. Properties of alumina/chromia scales in N2-containing low oxygen activity environment investigated by experiment and theory

Two types of models were employed here, slab (surface) and bulk models. The calculations employed ultrasoft pseudopotentials generated on-the-fly with 500 eV energy cut-off, and were spin-polarized throughout. A k-point mesh with 0.04 Å^{-1} mesh distance was used. The convergence criteria included 10^{-5} eV/atom for the energy and 10^{-3} Å displacement. For bulk calculations, lattice parameters were relaxed in addition to the geometry optimization.

5.2.1 Method validation

The chosen parameters were tested by computing the relative stabilities of the Al_2O_3 and Cr_2O_3 couple, as well as the AlN and CrN couple:

$$Cr_2O_3(s) + 2Al(s) \rightarrow Al_2O_3(s) + 2Cr(s) \tag{5.1}$$

for which the experimental enthalpy is $\Delta H_{exp} = \Delta H_f[Al_2O_3] - \Delta H_f[Cr_2O_3]$ = -535 kJ/mol compared to ΔH_{DFT} = -495 kJ/mol and

$$CrN(s) + Al(s) \rightarrow Cr(s) + AlN(s) \tag{5.2}$$

for which $\Delta H_{exp} = \Delta H_f[AlN] - \Delta H_f[CrN]$ = -201 kJ/mol and ΔH_{DFT} = -191 kJ/mol. ΔH_{DFT} is computed as the difference in total energy between the products and reactants:

$$\Delta H_{DFT} = \sum_{p=prod} E_{tot}[p] - \sum_{r=react} E_{tot}[r] \tag{5.3}$$

The computed enthalpies are deemed satisfactory with regards to the experimental values.

Slab calculations

Both the alumina and chromia slabs are formed by cleaving a unit cell (corondum structure containing 12 M = Cr, Al and 18 O) along the (001) direction and adding a 10 Å vacuum slab along the C-direction. The geometry optimized structures are shown in Fig. 5.1. The slab contains two coordinately unsaturated metal sites (CUS), which are denoted [-,-]. Thus [-,O], or [O,-] would imply that one of the two sites is occupied by oxygen. The calculations performed here are of the general reaction:

$$MN(s) + [-;A]M_{2x}O_{3x}(slab) \rightarrow M(s) + [N;A]M_{2x}O_{3x}(slab) \tag{5.4}$$

where M=Al, Cr and A=-, N, or O, denoting whether the CUS site is vacant or occupied by nitrogen or oxygen. The reaction enthalpy is calculated from Eq. 5.3. The experimental enthalpy of formation of $MN(s)$ is used to shift the calculated enthalpy to arrive at the more relevant surface nitridation enthalpy, denoted with a tilde:

$$\Delta \widetilde{H}_M^{N;-} = \Delta H_M^{N;-} - \Delta H_{exp}[MN(s)] \tag{5.5}$$

The reaction in this case becomes:

$$\frac{1}{2}N_2 + [-;A]M_{2x}O_{3x}(slab) \rightarrow [N;A]M_{2x}O_{3x}(slab) \tag{5.6}$$

And analogously for the case:

$$2MN(s) + [-;-]M_{2x}O_{3x}(slab) \rightarrow 2M(s) + [N;N]M_{2x}O_{3x}(slab) \tag{5.7}$$

Bulk calculations

The bulk models can be split up into pure and doped materials. The pure materials include metals, metal nitrides and metal oxides:

- Metals: Al - FCC, Cr - BCC
- Nitrides: AlN - Wurtzite structure, CrN - NaCl structure
- Oxides: Al_2O_3 and Cr_2O_3 - both corundum structure with 12 M (Al, Cr) and 18 O in the unit cell

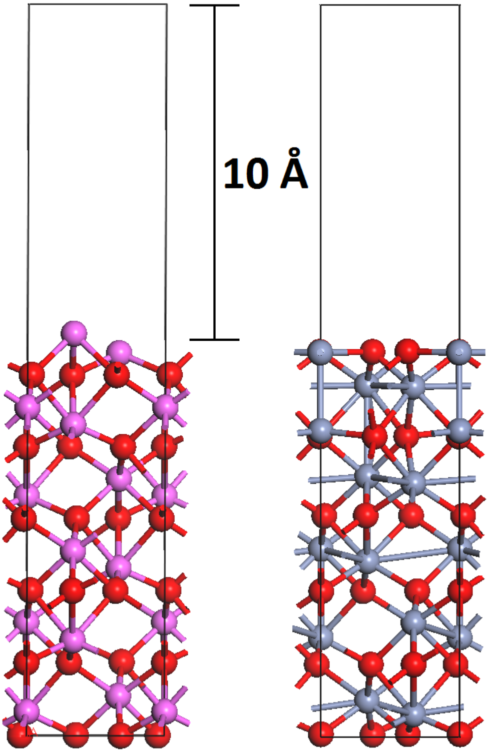

Figure 5.1: One unit cell of chromia (left) and alumina (right) is cleaved along the (001) plane and a 10 Å vacuum slab is added on top, along the C-axis. The figures show relaxed structures of the two oxides.

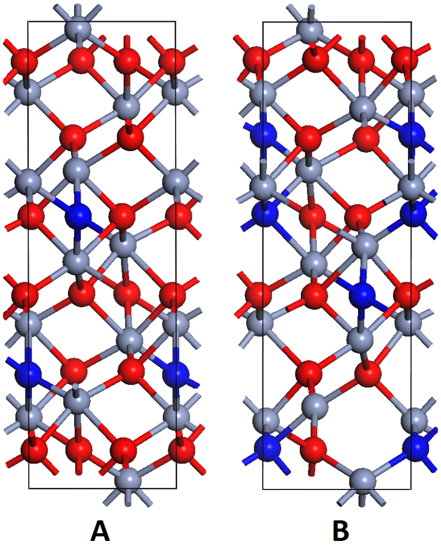

Figure 5.2: One unit cell of chromia in which two oxygen atoms are substituted to nitrogen and one oxygen vacancy is created. The two structures show two different possible permutations of forming these oxy-nitrides. The energies differ by around 0.03 eV which is negligible.

For these materials, the unit cell was relaxed along with the lattice parameters using the earlier mention computational parameters.

The doped materials are oxy-nitrides which are formed by substitutional nitrogen-doping in chromia. To maintain charge balance one oxygen atom is removed for every two nitrogen in the unit cell. To see if the calculations are stable with respect to different permutations of the oxy-nitrides, two structures were relaxed and their energies compared, see Fig. 5.2. The energies differ by 0.03 eV and the structures are deemed stable.

5.3 B. Fates of hydrogen during alumina growth at low partial pressures of water

The computational parameters employed in this paper are similar to those of Sec. 5.3 with the exception that they employed 550 eV energy cut-off, no spin-polarized calculations and the grain-boundary calculations included a dispersion correction as developed by [44].

Bulk and slab models were employed. Slab models are taken to be bulk models which have been cleaved along a direction and where a vacuum slab has been added onto the cleaved surface.

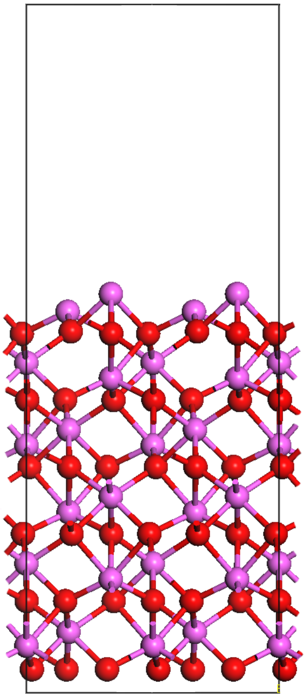

Figure 5.3: Slab model of all-Al//all-O illustrating two extreme conditions, 0% and 100% oxygen coverage.

Slab calculations

The alumina slab was created by cleaving a 2x2x1 supercell of alumina along the (001) direction. The cut was made to be able to sustain two 50% oxygen covered surfaces (labeled: half-Al/half-O), or alternatively, a slab where one surface has 100% oxygen coverage, and the other is aluminium terminated (labeled: all-Al//all-O), both with a 10 Å vacuum slab, see Fig. 5.3.

Furthermore, grain boundary models, obtained by closing the vacuum slab were employed. All lattice parameters were subsequently relaxed, which is not the case for the free standing slabs.

Bulk and molecule calculations

Bulk models employed include Al and Al_2O_3. H_2 and H_2O molecules were computed in large vacuum slabs.

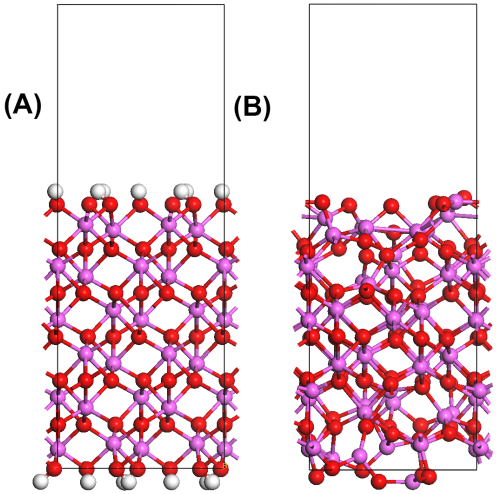

Figure 5.4: Slab models of (A) hydroxylated alumina slab, and (B) half-All/half-O slab.

Surface energy calculations

The surface energy was computed for various slabs to compare interface terminations. It is defined as:

$$\Delta E_{surf} = \frac{E_{slab} - nE_{bulk}}{2A} \tag{5.8}$$

where n is the number of M_2O_3 formula units in the slab model and A is the slab interface area. For hydroxylated slabs, this equation becomes:

$$\Delta E_{surf,OH} = \frac{E_{slab} - (nE_{bulk} + mE_{H_2O})}{2A} \tag{5.9}$$

where m is the number of water molecules required to terminate both slab interfaces.

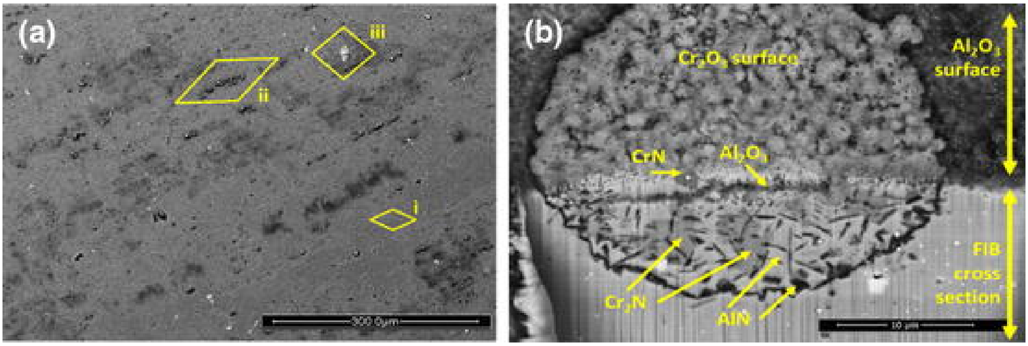

Figure 6.1: SEM images of the FeCrAl(RE) alloy after a one week exposure. (a) Top view image showing the alumina base oxide (i), a chromia rich patch (ii), and a reactive element particle (iii). (b) Cross-section of the chromia nodule showing internal nitridation.

6 Results and Discussion

Results obtained from exposures and SEM analysis are presented first, as they are required to build an understanding of the problem. Internal nitridation beneath alumina and chromia scales is the subject of paper A, and presented in Sec. 6.2. Sec. 6.3 covers hydroxylated alumina surfaces and grain-boundaries.

6.1 Exposure results

A FeCrAl(RE) alloy has been exposed in 95% N_2, 5% H_2 atmosphere with ppm content of water for 168 h at 900 °C. The alloy contains nominally 21.0% Cr, 5.0% Al, 3.0% Mo, small amounts of Y, Hf, and Zr, and Fe in balance. The oxygen activity in this atmosphere is very low, but enough to oxidize aluminium and form a protective barrier oxide. Chromia domains were found on the surface, possibly formed on chromium carbides, beneath which nitridation had occurred (Fig. 6.1 center). The nitridation effect seen in these alloys, as visualized in Fig. 6.1, is that alumina appears to be inert to nitrogen, while internal nitridation is observed beneath the chromia nodule. This is discussed in Sec. 6.2. The effect of water acting as oxidant is discussed in Sec. 6.3.

6.2 Properties of alumina/chromia scales in N2-containing low oxygen activity environment investigated by experiment and theory

Paper B discusses necessary conditions for N_2 dissociation on alumina and chromia surfaces. N_2 dissociation on two surface conditions were studied, 0%, and 50% oxygen coverage. Considering that nitridation is observed beneath chromia scales and not alumina, the surface is an interesting starting point.

6.2.1 Necessary conditions for N2 dissociation

Employing the earlier notations, the adsorption energy of nitrogen on alumina and chromia, i.e.:

$$\frac{1}{2}N_2 + [-;-]M_{2x}O_{3x}(slab) \rightarrow [N;-]M_{2x}O_{3x}(slab) \tag{6.1}$$

is found to be $\Delta\widetilde{H}_{Al}^{N;-}$ = -28.1 kJ/mol and $\Delta\widetilde{H}_{Cr}^{N;-}$ = -141 kJ/mol. Noting that the entropy contribution for N_2 is around 0.2 kJ/(mol K) renders N_2 dissociation on Al CUS sites non-spontaneous by around 180 kJ/(mol N_2) at 900 °C. The same analysis gives a dissociation energy on chromia of about -40 kJ/(mol N_2), exothermic.

To test the sensitivity of surface coverage of oxygen, calculations with 50% coverage are considered, see the following reaction:

$$\frac{1}{2}N_2 + [-;O]M_{2x}O_{3x}(slab) \rightarrow [N;O]M_{2x}O_{3x}(slab) \tag{6.2}$$

Here, $\Delta\widetilde{H}_{Al}^{N;O}$ = +39.1 kJ/mol and $\Delta\widetilde{H}_{Cr}^{N;O}$ = -135 kJ/mol. Instead of nitrogen and oxygen occupying one CUS site each, on alumina there is NO formation, implying an inability to co-chemisorb N and O to the alumina surface.

Finally, to see the effect of full N coverage, the same calculations were performed with all sites occupied by N:

$$N_2 + [-;-]M_{2x}O_{3x}(slab) \rightarrow [N;N]M_{2x}O_{3x}(slab) \tag{6.3}$$

Results show $\Delta\widetilde{H}_{Al}^{N;N}$ = -93.9 kJ/mol and $\Delta\widetilde{H}_{Cr}^{N;N}$ = -135 kJ/mol. In this case there is residual N-N bonding which adds to the stability on alumina. On chromia however, there is complete dissociation.

Note here that there is a bottleneck for the chemisorption on chromia as 100% N coverage shows half the exothermicity of the 50% coverage. Taking the entropy contribution at 900 °C (+240 kJ/(mol N_2)), an endothermicity of +105 kJ/mol is arrived at for 100 % N-coverage [N,N], compared to -40 kJ/mol for 50 % N-coverage 2[N,-].

There is a fundamental differences between alumina, and chromia scales and the availability of CUS sites. It is crucial for the surface to have available CUS sites in order to allow nitrogen adsorption and dissociation. Chromia, unlike alumina is known to have several oxidation numbers, such as Cr(III)→Cr(IV) allowing it to donate electrons for N_2 dissociation, which requires 6 electrons. Additionally, there are two driving forces for maintaining a high CUS covered chromia surface:

Firstly, the superior stability of alumina ($\Delta H_f(Al_2O_3)$=-1675 kJ/mol) compared to chromia ($\Delta H_f(Cr_2O_3)$=-1134 kJ/mol) implies that as long as there is aluminium in the vicinity of the chromia, aluminium in the alloy can reduce chromia. Secondly, the drive for internal nitridation of aluminium whereby AlN is formed ($\Delta H_f(AlN)$=-318 kJ/mol, compare with $\Delta H_f(CrN)$=-117 kJ/mol), will work to incorporate nitrogen into chromia.

6.2.2 Nitrogen incorporation through chromia scales

In the previous section, chromia scales were shown to be more likely to chemisorb and dissociate N_2. The next step in order to nitride the alloy beneath the chromia scale is to transport nitrogen ions through the chromia lattice. Here investigated in the form of transient chromium oxy-nitrides.

As long as there is unreacted Al in the vicinity of the chromia patch that can reduce it, there will be no build up of any barrier chromium oxy-nitride. This chromium oxy-nitride which is required for nitrogen diffusion through the bulk is represented by the following reaction:

$$Cr_2O_3(s) + \frac{y}{2}N_2(g) + yAl(s) \rightarrow Cr_2N_yO_{3-\frac{3y}{2}}(V_O^{**})_{\frac{y}{2}}(s) + \frac{y}{2}Al_2O_3(s) \tag{6.4}$$

Chromia can be thought of as to be in contact with two media, N_2 gas and Al in the alloy, since Cr and Fe can not reduce chromia. Nitrogen reacts with chromia to form oxy-nitride and the left-over oxygen subsequently reacts with Al to form alumina. The stability of this chromium oxide is calculated relative to AlN:

$$Cr_{12}O_{18}(s) + 2AlN(s) \rightarrow Cr_{12}N_2O_{15}(V_O^{**})(s) + Al_2O_3(s) \tag{6.5}$$

The reaction enthalpy is $\Delta H_r = +123$ kJ/mol. By adding the enthalpy of formation of 2 AlN ($\Delta H_f(Al) = -318$ kJ/mol) $\Delta H_r =$ -514 kJ/mol is arrived at for the reaction:

$$N_2(g) + Cr_{12}O_{18}(s) + 2Al(s) \rightarrow Cr_{12}N_2O_{15}(V_O^{**})(s) + Al_2O_3(s) \tag{6.6}$$

A plateau is in sight as the following further Al_2O_3 driven reaction:

$$N_2(g) + Cr_{12}N_2O_{15}(V_O^{**})(s) + 2Al(s) \rightarrow Cr_{12}N_4O_{12}(V_O^{**})_2(s) + Al_2O_3(s) \tag{6.7}$$

has a reaction enthalpy of $\Delta H_r =$ -570 kJ/mol. The limiting case, CrN formation is exothermic by $\Delta H_r =$ -750 kJ/mol:

$$N_2(g) + Cr_2O_3(s) + 2Al(s) \rightarrow 2CrN(s) + Al_2O_3(s) \tag{6.8}$$

A reason why the transient chromium oxy-nitride has not been found experimentally is that it disproportions into CrN and Cr_2O_3:

$$Cr_{12}N_2O_{15}(V_O^{**})(s) \rightarrow 5Cr_2O_3(s) + 2CrN(s) \tag{6.9}$$

which is exothermic, $\Delta H_r = \sim$-200 kJ/mol. The results are summarized in the energy landscape in Fig. 6.2.

6.3 Fate of hydrogen in hydroxylated alumina grain-boundaries

So far, the surfaces under study have been oxygen covered, but considering that the oxidant is not pure oxygen, but water, the surface could be hydroxide terminated. The

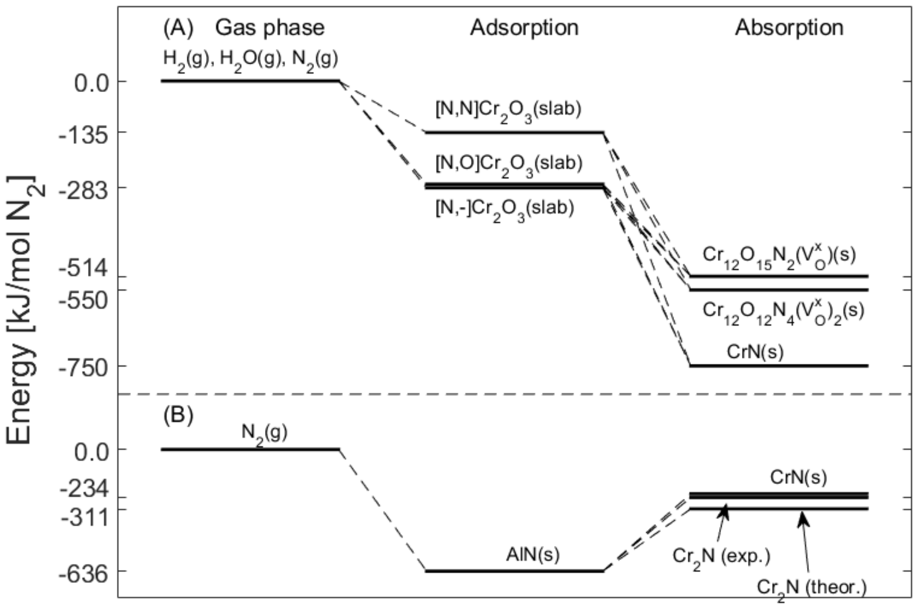

Figure 6.2: (A) Energy landscape for N_2 incorporation into the alloy to by forming transient chormium oxy-nitrides. (B) Net nitridation enthalpies of aluminium and chromium, once there is a nitridation path available.

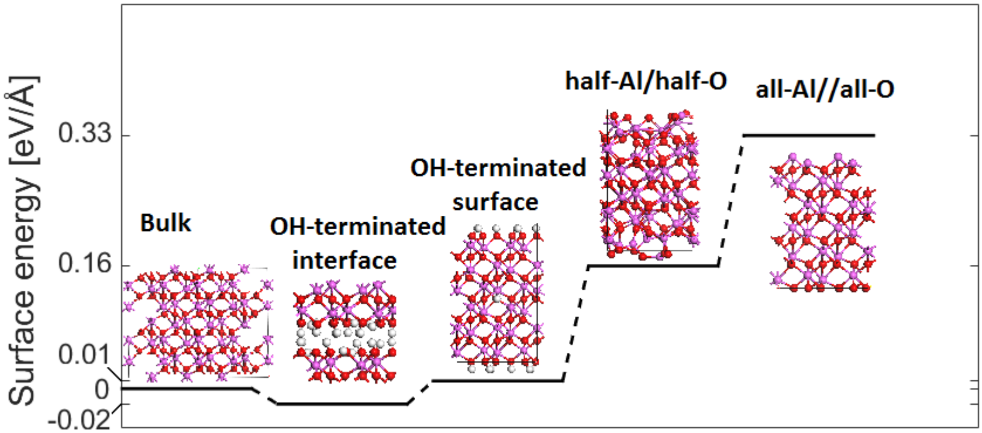

Figure 6.3: Computed surface energies for hydroxylated and unhydroxylated surface slabs, relative to bulk alumina.

surface energies have been calculated for different slabs, as well as a hydroxylated grain boundary, see Fig. 6.3.

The hydroxylated surfaces are more stable than the oxygen/metal terminated surfaces. There is thus reason to believe that alumina surfaces are in fact hydroxylated, making it more difficult than it already is to dissociate N_2, chromia on the other hand maintains a steady CUS coverage on its surface due to there being a driving force to e.g. oxidize and nitride aluminium, but when the driving force is removed, chromia also forms a protective scale.

The understanding of the oxidation process involves three steps:

1. Oxygen vacancies are formed at the oxide/alloy interface and diffuse to the surface.
2. Hydroxide oxygen diffuses into the vacancy, leaving a hydride to accommodate the surface oxygen vacancy.
3. Re-hydroxylation of the vacant surface state by H_2O whereby, (A) H_2 evolves through H^--H^+ recombination, or (B) the surface hydride enters an oxygen vacancy.

It is important to note that to maintain a steady oxidation process through a hydroxylated surface, requires disposal of the cathode product i.e. hydrogen, by hydrogen evolution or by incorporating hydrogen into the oxide scale.

To start off, to oxidize aluminium with hydroxide oxygen from the surface is exothermic, $\Delta E = -1.60$ eV:

$$\frac{2}{3}Al(s) + (OH)_{12}@Al_2O_3(slab) \rightarrow \frac{1}{3}Al_2O_3(s) + (OH)_{11}H@Al_2O_3(slab) \tag{6.10}$$

A subsequent hydrogen evolution by recombining the H^- with a vicinal proton is significantly endothermic, $\Delta E = 0.96$ eV:

$$(OH)_{11}H@Al_2O_3(slab) \rightarrow H_2(g) + (OH)_{10}O@Al_2O_3(slab) \tag{6.11}$$

Couple the hydrogen evolution with re-hydroxylation by water, in case of which it becomes exothermic, $\Delta E = -0.99$ eV:

$$H_2O(g) + (OH)_{11}H@Al_2O_3(slab) \rightarrow H_2(g) + (OH)_{12}@Al_2O_3(slab) \tag{6.12}$$

It appears as if the hydrogen evolution process becomes prohibited unless it occurs in conjunction with a re-hydroxylation process. The entropic contribution at 900 °C is large and the separate hydrogen evolution would be preferred at a free hydroxylated alumina surface.

Consider the following hydrogen pickup reaction:

$$H_2O(g) + (OH)_{11}H@Al_2O_3(V_O)_2(slab) \rightarrow (OH)_{12}@Al_2O_3(H@V_O)_2(slab) \tag{6.13}$$

The reaction enthalpy is $\Delta E = -0.26$ eV, it's tempting to conclude that this channel for disposing hydrogen is superior to the hydrogen evolution channel. It must be mentioned that the hydrogen incorporation renders extrinsic surface states accessible. Given that GGA underestimates the band gap, these results must be met with caution. Studying

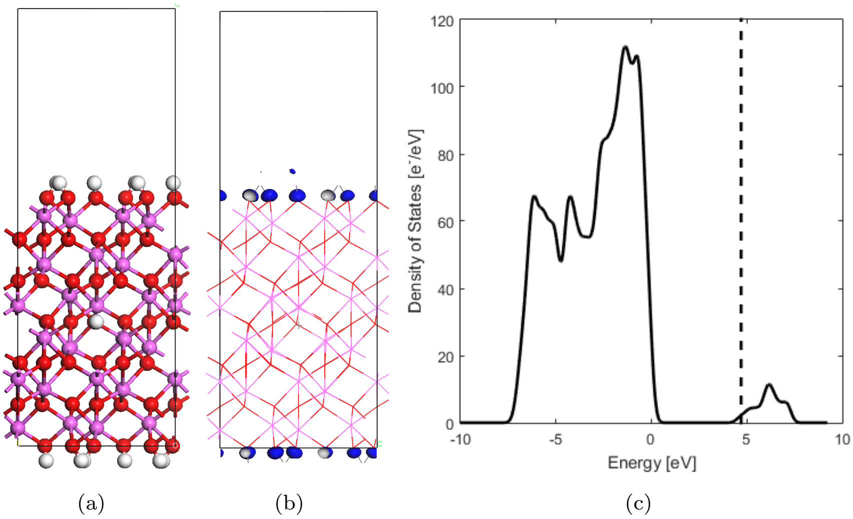

(a)
(b)
(c)

Figure 6.4: (A) Hydroxylated free standing slab model with a hydride ion incorporated into the lattice. (B) Highest occupied molecular orbital (HOMO) seen to occupy extrinsic surface states. (C) The density of states (DOS) shows the extrinsic states to occupy the conduction band, about 4.5 eV above the valence band.

the grain boundary interface, we note that the band gap is 1.5 times larger than in the free standing slab, here the extrinsic states are inaccessible and a reaction enthalpy of $\Delta E = +1.47$ eV is acquired:

$$H_2O(g) + (OH)_{11}H@Al_2O_3(V_O)_2(GB) \rightarrow (OH)_{12}@Al_2O_3(H@V_O)_2(GB) \qquad (6.14)$$

Fig. 6.4 and Fig. 6.5 show the highest occupied molecular orbitals (both visualized and as a density of states plot) for a free standing hydroxylated slab and for a hydroxylated grain boundary model.

The conclusion is that there is no hydrogen pick-up into the oxide lattice, neither at the grain-boundary nor at the gas-oxide interface. If hydrogen is to be found, then it is at this interface or at grain-boundaries, in the form of hydroxide or hydrides. A possible channel for disposing hydrogen may instead be pick-up into the alloy at the oxide-alloy interface.

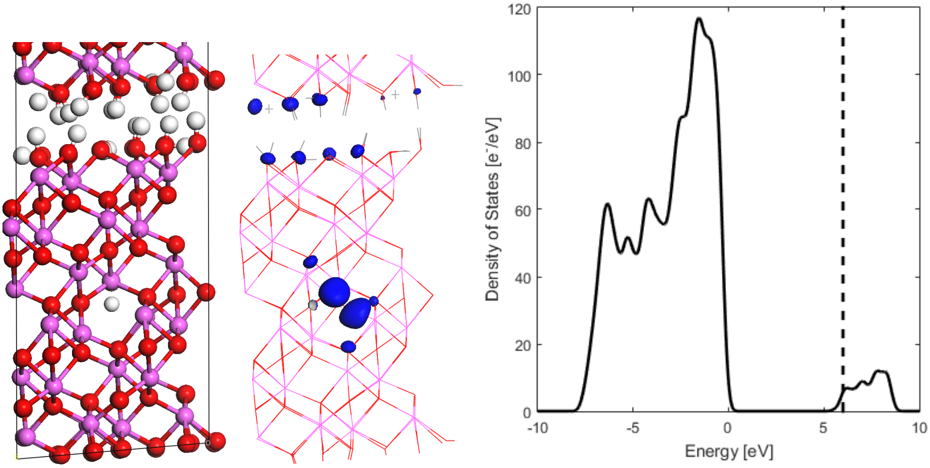

(a) (b) (c)

Figure 6.5: (A) Hydroxylated grain boundary model with a hydride incorporated into the lattice. (B) Highest occupied molecular orbital (HOMO) states distributed to vacancy and surface states. (C) The density of states (DOS) shows the HOMO to reside in extrinsic states in the conduction band, about 6 eV above the valence band.

7 Summary and future work

This thesis attempts at addressing two generic features present in high temperature corrosion; (i) transport of an oxidant through different barrier oxides, and (ii) interface hydroxylation and fate of hydrogen when H_2O acts as oxidant. As a last point, (iii) future work on bridging Wagner theory of oxidation and Cabrera-Mott theory of oxide growth by Marcus theory of electron transport is discussed.

(i) Chromia nodules are found in an otherwise protective alumina scale on a FeCrAl(Re) alloy. Under high nitrogen, low $p(O_2)$ conditions, chromia nodules permeate nitrogen, unlike alumina. A fundamental difference between the two was found with respect to their surface chemistry i.e. the availability of CUS sites which are crucial for N_2 dissociation. Six electrons are required to dissociate nitrogen, favoring chromia as it is known for its oxidation states Cr(III)→Cr(IV), while alumina maintains an oxidation state of (III). Furthermore chromia is less noble, meaning that aluminium in the alloy can reduce chromia. As long as there is available aluminium in the vicinity of the chromia, a barrier oxide is not formed, and a meta-stable chromium oxy-nitride can be maintained. Future work will address internal carburization and carbon transport through oxide scales.

(ii) Water may act as an oxidant, and as such will hydroxylate interfaces as to minimize interface energies. Upon oxidation of the metal, hydrogen must be disposed of, either as H_2 at the interfaces or hydrides in oxygen vacancies in the oxide lattice or as hydrides in oxygen vacancies at interfaces. Calculations show there to be no driving force to form H_2 in interfaces, nor any disposal of hydrides into vacancies in the oxide lattice. The former due to confinement effects owing to the grain-boundary. If hydrides are to be found, it is in oxygen vacancies at interfaces . Alternatively, hydrogen could be disposed of in the alloy. Future work will address if and how hydride incorporation is affected by reactive elements in grain-boundaries.

(iii) This concerns a subject that has not been formulated in this work but which is highly relevant is electron transport through large band-gap oxide scales. Following Wagner theory of oxidation, transport of oxygen vacancies, as well as electron transport take crucial roles in the growth of oxides. Alumina typically follows parabolic growth rate, and as such the rate limiting step is not taken to be electron transport but rather that of the ions. Schottky defects are expected to be the most common defect type in alumina due to their low formation enthalpy. These charged oxygen vacancies may offer a transport path for electrons via a inter-site tunneling and resulting Cabrera-Mott like ion mobility. Here we aim to contribute a bridge between Wagner theory and Cabrera-Mott theory with Marcus theory to describe the electron transport in large band-gap oxides.

The theory-experiment collaboration has shown to be fruitful, as working from two different points-of-view contribute with different outlooks on the issues. With experiment, the problems in modern alloy design are uncovered, and together with advanced analysis methods a lot of these issues can be resolved and understood. With theory and first-principle simulations it is possible to go deeper into the atomic processes and find basic mechanisms which are responsible for the observed effects.

Acknowledgements

First and foremost, I would like to acknowledge my supervisors, Itai and Torbjörn for their help and tutoring during my time here. I think our collaboration has been improving since day one.

Jan-Erik and Lars-Gunnar, thank you for helping when needed. I still remember when I went for the (surprise) interview, and Jan-Erik asked me if I'm nervous, to which I replied that I wasn't even aware of it being an interview (Itai had told me I was just coming to have a look around).

I would like to thank Patrik for our gym sessions, which help me stay motivated in front of the computer (at least that's what I fool myself to think). Julien, thank you for telling me about your temperature profile measurements which will hopefully lead to an automatic temperature profile measurement machine, which I have been developing ever since together with Patrik. Robin, Hannes, Christine, und Claudia, danke, ohne euch würde ich nicht so gut Deutsch sprechen. Valentina, thank you for being one of few theoretical chemists, so I don't have to travel alone to theoretical chemistry meetings. I would like to acknowledge the High Temperature Corrosion center (HTC) for the collaboration and discussions resulting in the published papers. A big thanks to Marlene, thank you for being supportive of my work and hobbies, always, and giving me advice whenever I need it. I'm dearly thankful to my parents, my sister and her family, and my brother for being there for me when it gets tough.

Last but not least, thank you to all my colleagues for making this a happy working place.

References

[1] C. Geers et al. Properties of Alumina/Chromia Scales in N2-Containing Low Oxygen Activity Environment Investigated by Experiment and Theory. *Oxidation of Metals* (2017). DOI: `10.1007/s11085-016-9703-3`.

[2] V. Babic et al. Fates of Hydrogen During Alumina Growth Below Yttria Nodules in FeCrAl(RE) at Low Partial Pressures of Water. *Electrocatalysis* (Mar. 2017). ISSN: 1868-5994. DOI: `10.1007/s12678-017-0368-8`. URL: `https://doi.org/10.1007/s12678-017-0368-8`.

[3] P. Hou. Impurity Effects on Alumina Scale Growth. *Journal of the American Ceramic Society* **86**.4 (2003), 660–68. DOI: `10.1111/j.1151-2916.2003.tb03355.x`.

[4] A. H. Heuer et al. Alumina Scale Formation: A New Perspective. *Journal of the American Ceramic Society* **94**.S1 (2011), 146–153. DOI: `10.1111/j.1551-2916.2011.04573.x`.

[5] P. Kofstad. *High Temperature Corrosion.* Elsevier Applied Science Publishers LTD, 1988.

[6] F. H. Stott, G. C. Wood, and J. Stringer. The Influence of Alloying Elements on the Development and Maintenance of Protective Scales. *Oxidation of Metals* **44**.1 (1995), 113–145.

[7] A. Atkinson. Grain-boundary Diffusion : An Historical Perspective. *Journal of the Chemical Society, Faraday Transactions, Volume 86* (1990), 1307–1310.

[8] P. Sarrazin et al. *Mechanisms of High Temperature Corrosion: A Kinetic Approach.* Trans Tech Publications Ltd., 2008.

[9] C. Badini and F. Laurella. Oxidation of FeCrAl alloy: Influence of temperature and atmosphere on scale growth rate and mechanism. *Surface and Coatings Technology* **135**.2-3 (2001), 291–298. ISSN: 02578972. DOI: `10.1016/S0257-8972(00)00989-0`.

[10] A. Atkinson. Wagner Theory and Short Circuit Diffusion. *Materials Science and Technology* **4**.December (1988), 1046–1051.

[11] A. Heuer et al. On the growth of Al2O3 scales. *Acta Materialia* **61**.18 (2013), 6670–6683. ISSN: 13596454. DOI: `10.1016/j.actamat.2013.07.024`. URL: `http://dx.doi.org/10.1016/j.actamat.2013.07.024`.

[12] G. Tammann. Uber Anlauffarben von Metallen. *Z. Anorg. Chem.* **111** (1920), 78.

[13] N. Pilling and R. Bedworth. The Oxidation of Metals at High Temperatures. *J. Inst. Met.* **29** (1923), 529–591.

[14] F. Morin, G. Beranger, and P. Lacombe. Limits of application for Wagner's oxidation theory. *Oxidation of Metals* **4**.78 (1972), 51–62. ISSN: 0030770X. DOI: `10.1007/BF00612507`.

[15] H. Josefsson et al. Oxidation of FeCrAl alloys at 500–900 ° C in dry O_2. *Materials and Corrosion* **56**.11 (2005), 801–805.

[16] W. J. Quadakkers et al. Growth Rates of Alumina Scales on Fe–Cr–Al Alloys. *Oxidation of Metals* **61**.1 (2004), 17–37. ISSN: 1573-4889. DOI: `10.1023/B:OXID.0000016274.78642.ae`. URL: `http://dx.doi.org/10.1023/B:OXID.0000016274.78642.ae`.

[17] W. J. Quadakkers et al. Growth Rates of Alumina Scales on Fe–Cr–Al Alloys. *Oxidation of Metals* **61**.1 (2004), 17–37. ISSN: 1573-4889. DOI: `10.1023/B:OXID.0000016274.78642.ae`. URL: `http://dx.doi.org/10.1023/B:OXID.0000016274.78642.ae`.

[18] N. Birks, G. Meier, and F. Pettit. *Introduction to the high temperature oxidation of metals.* Cambridge University Press, 2006.

[19] N. Cabrera and N. F. Mott. Theory of the oxidation of metals. *Reports on Progress in Physics* **12**.1 (1949), 163–184. DOI: `10.1088/0034-4885/12/1/308`. arXiv: `arXiv:1011.1669v3`.

[20] F. Fehlner and N. Mott. "Oxidation in the Thin-Film Range". *Oxidation of Metals and Alloys.* Ed. by D. Douglass. American Society for Metals, 1970. Chap. 3, pp. 37–62.

[21] H. E. Evans, A. T. Donaldson, and T. C. Gilmour. Mechanisms of Breakaway Oxidation and Application to a Chromia-Forming Steel. *Oxidation of Metals* **52**.5 (1999), 379–402. ISSN: 1573-4889. DOI: `10.1023/A:1018855914737`. URL: `http://dx.doi.org/10.1023/A:1018855914737`.

[22] B. A. Pint and K. B. Alexander. Grain Boundary Segregation of Cation Dopants in a-Al2O3 Scales. *J. Electrochem. Soc.* **145**.6 (1998), 1819.

[23] B. Pint. Progress in Understanding the Reactive Element Effect Since the Whittle and Stringer Literature Review (). DOI: `10.1.1.136.734`.

[24] E. Schrödinger. Quantisierung als Eigenwertproblem. *Annalen der Physik* **384** (1926), 361–376. DOI: `10.1002/andp.19263840404`.

[25] M. Born and R. Oppenheimer. Zur Quantentheorie der Molekeln. *Annalen der Physik* **389** (1927), 457–484. DOI: `10.1002/andp.19273892002`.

[26] D. R. Hartree. The Wave Mechanics of an Atom with a Non-Coulomb Central Field. Part I. Theory and Methods. *Proceedings of the Cambridge Philosophical Society* **24** (1928), 89–110. DOI: `10.1017/S0305004100011919`.

[27] D. R. Hartree. The Wave Mechanics of an Atom with a Non-Coulomb Central Field. Part II. Some Results and Discussion. *Proceedings of the Cambridge Philosophical Society* **24** (1928), 111–132. DOI: `10.1002/andp.19273892002`.

[28] V. Fock. Naherungsmethode zur Losung des quantenmechanischen Mehrkorperproblems. *Zeitschrift für Physik* **61** (1930), 126–148. DOI: `10.1007/BF01340294`.

[29] J. Slater. Note on Hartree's Method. *Physical Review* **35** (1930), 210–211. DOI: `10.1103/PhysRev.35.210.2`.

[30] J. Slater. The Theory of Complex Spectra. *Physical Review* **34** (1929), 1293–1322. DOI: `10.1103/PhysRev.35.210.2`.

[31] W. Kohn and L. Sham. Self-Consistent Equations Including Exchange and Correlation Effects. *Physical Review* **140** (1965), A1133–A1138. DOI: `10.1103/PhysRev.140.A1133`.

[32] W. Kohn and L. Sham. One-Particle Properties of an Inhomogeneous Interacting Electron Gas. *Physical Review* **145** (1966), 561–567. DOI: `10.1103/PhysRev.145.561`.

[33] J. P. Perdew and Y. Wang. Accurate and simple analytic representation of the electron-gas correlation energy. *Physical Review B* **45** (1992), 13244–13249. DOI: `10.1103/PhysRevB.45.13244`.

[34] J. P. Perdew et al. Atoms, molecules, solids, and surfaces: Applications of the generalized gradient approximation for exchange and correlation. *Phys. Rev. B* **46** (11 Sept. 1992), 6671–6687. DOI: `10.1103/PhysRevB.46.6671`. URL: `http://link.aps.org/doi/10.1103/PhysRevB.46.6671`.

[35] J. P. Perdew, K. Burke, and M. Ernzerhof. Generalized Gradient Approximation Made Simple. *Physical Review Letters* **77** (1996), 3865–3868. DOI: `10.1103/PhysRevLett.77.3865`.

[36] P. Hasnip et al. Density functional theory in the solid state. *Phil. Trans. R. Soc. A* **372** (2014), 20130270. DOI: `10.1098/rsta.2013.0270`.

[37] C. Adamo and V. Barone. Toward reliable density functional methods without adjustable parameters: The PBE0 model. *Journal of Chemical Physics* **110** (1998), 6158–6170. DOI: `10.1063/1.478522`.

[38] A. Becke. Density-functional thermochemistry. III. The role of exact exchange. *Journal of Chemical Physics* **98** (1993), 5648–5652. DOI: `10.1063/1.464913`.

[39] P. Mori-Sanchez, A. Cohen, and W. Yang. Many-electron self-interaction error in approximate density functionals. *Journal of Chemical Physics* **125** (2006), 201102. DOI: `10.1063/1.2403848`.

[40] L. Versluis and T. Ziegler. The Determination of Molecular Structures by Density Functional Theory. The Evaluation of Analytical Energy Gradients By Numerical Integration. *Journal of Chemical Physics* **88** (1988), 322–328. DOI: `10.1063/1.454603`.

[41] J. Andzelm, R. Fournier, and D. Salahub. Analytical gradient of the linear combination of Gaussian-type orbitals-local spin density energy. *Journal of Chemical Physics* **90** (1989), 6371. DOI: `10.1063/1.456354`.

[42] N. Ashcroft and N. Mermin. *Solid State Physics*. Saunders Collage, 1976.

[43] D. Vanderbilt. Soft self-consistent pseudopotentials in a generalized eigenvalue formalism. *Physical Review B* **41** (1990), 7892–7895. DOI: `10.1103/PhysRevB.41.7892`.

[44] S. Grimme et al. A consistent and accurate ab initio parametrization of density functional dispersion correction (DFT-D) for the 94 elements H-Pu. *The Journal of Chemical Physics* **132**.15 (2010), 154104.